

## Supporting Information for

### **Design of Strong and Weak Intermolecular Interactions to Engineer Buried Interfaces in Inverted Wide-Bandgap Perovskite Solar Cells**

*Hui Li,<sup>a\*</sup> Davide Regaldo,<sup>a</sup> Chun-Sheng Jack Wu,<sup>a</sup> Mirko Prato,<sup>b</sup> Antonella Treglia,<sup>a</sup> Heyong Wang,<sup>a</sup> Wolfram Hempel,<sup>c</sup> Michele Sessoloc,<sup>d</sup> Yang Zhou,<sup>e</sup> Andrea Olivati,<sup>a</sup> Annamaria Petrozza<sup>a\*</sup>*

<sup>a</sup>Center for Nano Science and Technology@Polimi, Istituto Italiano di Tecnologia, via Rubattino 81, 20134 Milano, Italy

<sup>b</sup>Materials Characterization Facility, Istituto Italiano di Tecnologia, via Morego 30, 16163 Genova, Italy

<sup>c</sup>Zentrum für Sonnenenergie- und Wasserstoff-Forschung Baden-Württemberg (ZSW), Meitnerstr.1, 70563 Stuttgart, Germany

<sup>d</sup>Instituto de Ciencia Molecular, Universidad de Valencia, C/Catedrático J. Beltrán 2, 46980 Paterna, Spain

<sup>e</sup>Wuhan National Laboratory for Optoelectronics, Huazhong University of Science and Technology, Wuhan Hubei 430074, China

\*Corresponding authors. E-mail: hui.li@iit.it; annamaria.petrozza@iit.it.

## **Contents**

### **1. Experimental Section**

### **2. Supporting Table: Table S1 and S2**

### **3. Supporting Figures: Figure S1 to S28**

# 1. Experimental Section

**1.1 Materials:** Organic halide salts (MAI, FAI) were purchased from Greatcell Solar Materials. Ethylenediammonium diiodide (EDAI<sub>2</sub>), C<sub>60</sub> and BCP were purchased from Xi'an Polymer Light Technology. Me-PACz (>98.0%), PbI<sub>2</sub> (99.99%), and PbBr<sub>2</sub> (>98.0%) were purchased from Tokyo Chemical Industry. CsI (99.9%), Histamine (99.9%), DMF (99.8% anhydrous), DMSO (99.9% anhydrous), Chlorobenzene (99.8%, anhydrous), Isopropanol (99.8%, anhydrous) were purchased from Sigma-Aldrich.

**1.2 Perovskite Precursor Solution preparation:** 1.77 eV perovskite: 1.2 M FA<sub>0.83</sub>Cs<sub>0.17</sub>Pb(I<sub>0.6</sub>Br<sub>0.4</sub>)<sub>3</sub> precursor solution was prepared by mixing FAI, MAI, PbI<sub>2</sub>, PbBr<sub>2</sub>, PbSCN<sub>2</sub> with the molar ratio of 0.83:0.17:0.40:0.60:0.01 in co-solvent DMSO/DMF (1 mL, 1:3 volume ratio). 1.83eV perovskite: 1.2 M FA<sub>0.83</sub>Cs<sub>0.17</sub>Pb(I<sub>0.5</sub>Br<sub>0.5</sub>)<sub>3</sub> precursor solution was prepared by mixing FAI, MAI, PbI<sub>2</sub>, PbBr<sub>2</sub>, PbSCN<sub>2</sub> with the molar ratio of 0.83:0.17:0.32:0.71:0.01 in co-solvent DMSO/DMF (1 mL, 1:3 volume ratio). The perovskite precursor solution was stirred at the room temperature for overnight. Before using, the precursor solution was filtered by 0.22 μm PTFE filter.

**1.3 Device fabrication:** Patterned glass/ITO substrates were cleaned by detergent, deionized water, acetone, and isopropanol in 15 minutes ultrasonic bath respectively, and then dried with N<sub>2</sub> flow, followed by UV-Ozone treatment. NiO<sub>x</sub> (10 mg·mL<sup>-1</sup>) dissolved in deionized water was deposited on the ITO substrate by spin-coating at 3,000 rpm for 40 s and then annealed at 110 °C for 15 min in air. Then the samples were transferred into a nitrogen glovebox for deposition of the Me-4PACz and perovskite layers. Me-4PACz (0.33 mg·mL<sup>-1</sup>) or Hi-Me (3:1, 1.5:1, 1:1 molar ratio) were dissolved in ethanol and then deposited on the NiO<sub>x</sub> substrate by spin-coating at 4000 rpm for 30 s and then annealed at 100 °C for 10 min. The precursor solution was spin-coated onto the NiO<sub>x</sub>/Me-4PACz layer at 5000 rpm for 32 s, and chlorobenzene (290 μl) as antisolvent was rapidly dripped onto the spinning substrate over an interval of 1 s during the second spin-coating step at 5 s before the end of the procedure, and then annealed at 100 °C for 20 min. After thermal annealing, EDAI<sub>2</sub> (1 mg·mL<sup>-1</sup>) dissolved in isopropanol was spin-coated on the perovskite film at 5,000 rpm for 30 s, followed by thermal annealing at 100 °C for 5 min. The fabricated substrates were subsequently transferred to a vacuum chamber where 25 nm C<sub>60</sub> (deposition rate of 0.01 nm·s<sup>-1</sup>), 3 nm BCP (deposition rate of 0.01 nm·s<sup>-1</sup>) and 80 nm Au electrode were consecutively deposited by thermal evaporation on the above substrate to the perovskite solar cells.

**1.4 Characterization:** Bruker D8 Advance equipped with a Cu Kα1 (λ = 1.544060 Å) anode, operating at 40 kV and 40 mA was employed to conduct the X-ray diffraction (XRD) and grazing incidence XRD (GIXRD). Top-view and cross-sectional morphology images of perovskite films were recorded by Field emission scanning electron microscopy (Mira3, Tescan). Fourier transform infrared spectroscopy (NIREOS Hera), and X-ray photoelectron spectroscopy (Kratos Axis UltraDLD spectrometer) were conducted to elucidate the molecular interaction. Bruker BioScope Resolve atomic force microscope was used to record the AFM and KPFM images. Time-of-Flight Secondary Ion Mass Spectrometry (ToF-SIMS) was performed using a ToF-SIMS5 system from IONTOF. In addition to employing a Bi source for analysis, we utilized a Cs source for sputtering. This choice enables the simultaneous detection of both electropositive and electronegative elements by selecting Cs clusters, such as CsBr<sup>+</sup>, and CsI<sup>+</sup>. Moreover, Cs clusters exhibit a reduced matrix effect compared to single ions like Pb<sup>+</sup> or Sn<sup>+</sup>, enhancing detection accuracy. The analyzed area was 50 × 50 μm<sup>2</sup>, while the sputter crater generated by the Cs source measured 300 × 300 μm<sup>2</sup>. UV-vis absorption spectra were recorded by a spectrophotometer Lambda 1050, PerkinElmer. C. Transient absorption spectroscopy was performed in transmission geometry. The ionization energy of the samples was measured with Ambient Photoemission Spectroscopy (APS) using an APS02 system from KP Technology. A Light Conversion PHAROS femtosecond laser produced ~280 fs pulses at 1030 nm. Focusing these pulses into a thin sapphire plate generated a broadband white-light probe. For short delays (<5 ns), we obtained 515 nm pump light by frequency-doubling the fundamental output. For longer delays (>1 ns), a Q-switched Nd:YAG laser (Innolas Picolo) provided 532 nm pump light, synchronized electronically with femtosecond laser via an electronic delay. We acquired kinetic data by integrating centered at the main photo-bleach (PB) peak at the band edge. Hyperspectral photoluminescence mapping setup uses an upright fluorescence microscope (Nikon LV100 ND) to measure local photoluminescence. A 100x objective lens (Nikon T Plan EPI SLWD, N.A. = 0.6) focuses the excitation light onto the sample. The emitted photoluminescence is then collected through the same objective and analyzed using a translating-wedge-based birefringent interferometer, which helps capture detailed spectral information. The excitation density dependent PLQY measurement was pumped by a 515 nm pulsed laser generated by a Pharos femtosecond pulsed laser and an external noncollinear optical parametric amplifier and then collected with a Maya 2000 Pro visible spectrometer and a 680 nm long pass filter. The SCLC measurements were performed by Keithley 2420 source measurement unit under dark. The current density-voltage (*J-V*) characteristics were measured using a computer-controlled Keithley 2420 source meter, while the simulated Air Mass 1.5 Global (AM 1.5G) irradiance was supplied by a class AAA Newport solar simulator. The light intensity was calibrated with a silicon reference cell, and the active area of the device was defined using an illumination-shadowing mask with an area of 0.0935 cm<sup>2</sup>. For the solar cell stability tests, devices were placed in an Arkeo stability platform (Cicci Research, Italy) under nitrogen

flow with the temperature control exposed to simulated 1 sun illumination. They operated at their maximum power point (MPP) throughout the test. All cells were encapsulated prior to testing. Geometry optimization and frequency calculations were performed at the wb97xd/6-31g level using Gaussian16. The optimized structures were confirmed as minima through frequency analysis. Dipole moments were computed with the same wb97xd/6-31g method and basis set. Electrostatic potential (ESP) maps were generated using GaussView 6.0.

## 2. Supporting Table

**Table S1.** The PCE and  $V_{oc}$  of perovskite solar cells based on perovskite with bandgap >1.80 eV.

|    | <b>Bandgap (eV)</b> | <b>PCE (%)</b> | <b><math>V_{oc}</math> (V)</b> | <b>Reference</b>                                       |
|----|---------------------|----------------|--------------------------------|--|
| 1  | 1.80                | 17.00          | 1.250                          | <i>Adv. Mater.</i> <b>2023</b> , 35, 2211742.          |
| 2  | 1.80                | 16.94          | 1.270                          | <i>Nat. Commun.</i> <b>2023</b> , 14, 932.             |
| 3  | 1.81                | 19.58          | 1.350                          | <i>Nat. Energy</i> <b>2024</b> , 9, 411-421.           |
| 4  | 1.84                | 17.96          | 1.326                          | <i>Adv. Mater.</i> <b>2024</b> , 36, 2410692.          |
| 5  | 1.88                | 18.40          | 1.360                          | <i>Nature</i> <b>2024</b> , 635, 860-866.              |
| 6  | 1.85                | 18.10          | 1.360                          | <i>Adv. Mater.</i> <b>2024</b> , 36, 2306568.          |
| 7  | 1.92                | 16.23          | 1.390                          |  |
| 8  | 1.85                | 19.00          | 1.379                          | <i>Angew. Chem. Int. Ed.</i> <b>2025</b> , e202501764. |
| 9  | 1.86                | 18.52          | 1.366                          | <i>Joule</i> <b>2024</b> , 8, 1-16.                    |
| 10 | 1.88                | 18.40          | 1.360                          | <i>Nature</i> <b>2024</b> , 635, 860-866.              |
| 11 | 1.93                | 16.90          | 1.422                          | <i>Nature</i> <b>2024</b> , 628, 306-312.              |
| 12 | 2.00                | 9.40           | 1.400                          | <i>Nat. Commun.</i> <b>2024</b> , 15, 9069.            |
| 13 | 2.00                | 13.41          | 1.312                          | <i>Nature</i> <b>2023</b> , 618, 74-79.                |
| 14 | 1.83                | 18.69          | 1.320                          | <i>Adv. Mater.</i> <b>2025</b> , 37, 2411027.          |
| 15 | 1.83                | 18.96          | 1.320                          | <i>Nat. Energy</i> <b>2024</b> , 9, 592-601.           |
|    | <b>1.83</b>         | <b>18.99</b>   | <b>1.364</b>                   | <b>This work</b>                                       |

**Table S2.** The comparison of PCE and operational stability of devices based on the perovskite with bandgap of 1.75~1.80 eV.

|    | <b>Bandgap (eV)</b> | <b>PCE (%)</b> | <b>Operational stability (ISOS-II protocol)</b> | <b>Reference</b>  |
|----|---------------------|----------------|---|---|
| 1  | 1.77                | 19.66          | 86%~300 hours                                   | <i>Small</i> <b>2023</b> , 19, 2303213.                         |
| 2  | 1.77                | 17.17          | 70%~3000 hours<br>( $\approx$ 90%~1000 hours)   | <i>ACS Energy Lett.</i> <b>2023</b> , 8, 3852-3859.             |
| 3  | 1.79                | 20.06          | 96%~913 hours                                   | <i>Adv. Funct. Mater.</i> <b>2024</b> , 34, 2308908.            |
| 4  | 1.77                | 19.40          | 92.1%~500 hours                                 | <i>ACS Energy Lett.</i> <b>2024</b> , 9, 1984-1992.             |
| 5  | 1.77                | 19.30          | 80%~337 hours                                   | <i>Adv. Energy Mater.</i> <b>2024</b> , 14, 2304429.            |
| 6  | 1.79                | 21.02          | 80%~620 hours                                   | <i>Adv. Funct. Mater.</i> <b>2024</b> , 2419393.                |
| 7  | 1.78                | 19.60          | 95%~1060 hours                                  | <i>Nat. Commun.</i> <b>2023</b> , 14, 7118.                     |
| 8  | 1.75                | 20.08          | 90%~2500 hours<br>( $\approx$ 92%~1000 hours)   | <i>Nat. Commun.</i> <b>2024</b> , 15, 8899.                     |
| 9  | 1.77                | 18.88          | 80%~427 hours                                   | <i>Energy Environ. Sci.</i> , <b>2024</b> , 17, 202-209.        |
| 10 | 1.77                | 19.50          | 95%~550 hours                                   | <i>Energy Environ. Sci.</i> , <b>2025</b> , 10.1039/D4EE02898H. |
|    | <b>1.77</b>         | <b>20.34</b>   | <b>95.5%~1000 hours</b>                         | <b>This work</b>  |

### 3. Supporting Figures

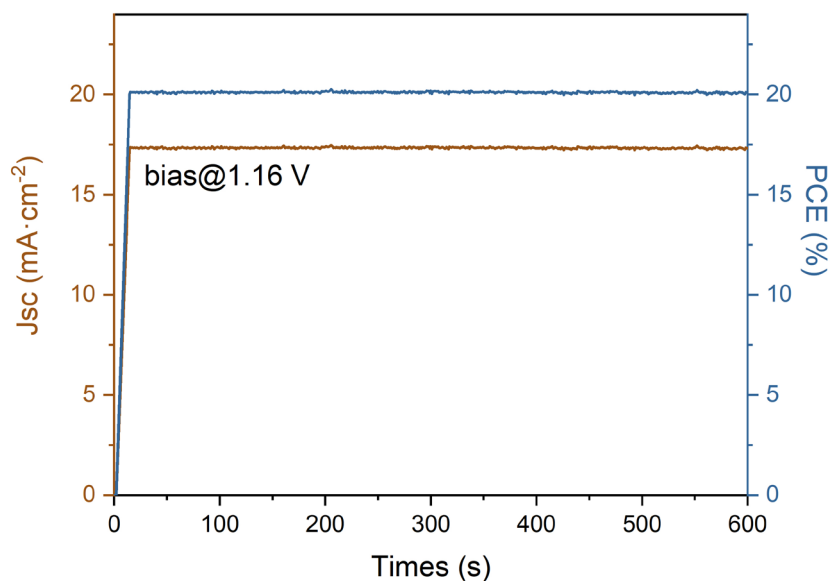


**Figure S1.** Steady-state output performance of champion 1.77 eV WBG PSCs.

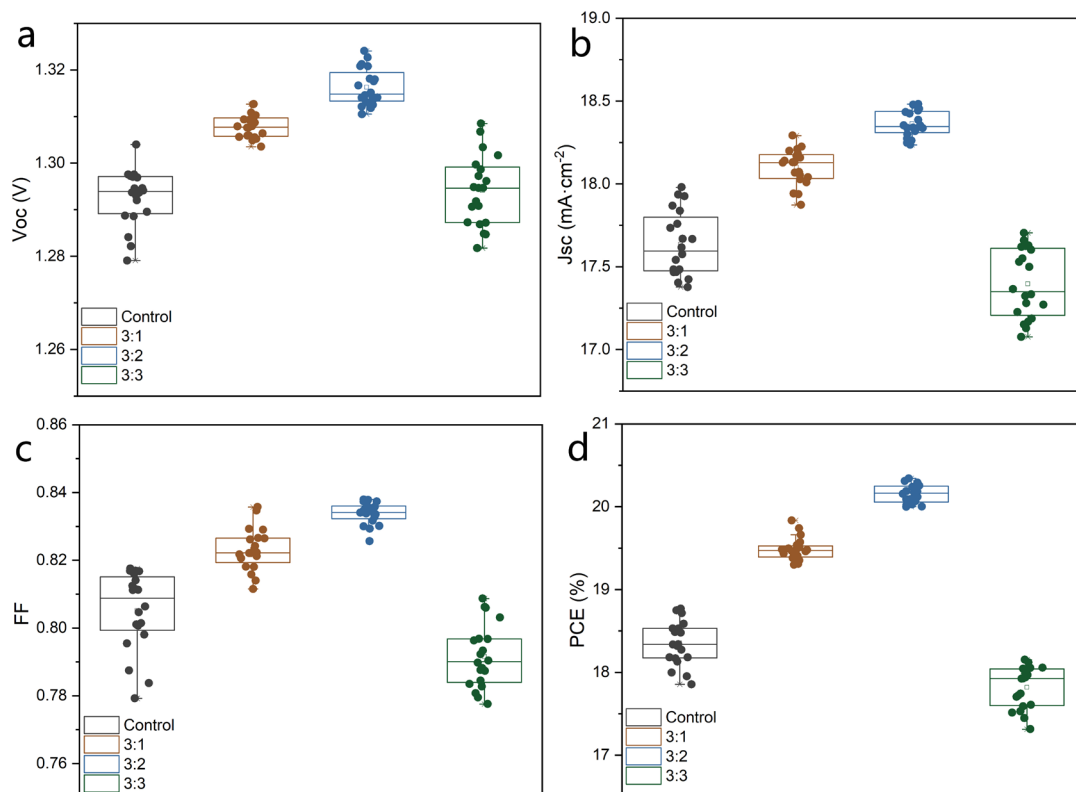


**Figure S2.** Statistical distributions of 1.77 eV-based WBG PSCs with different ratio of Me-4PACz: to histamine: (a)  $V_{oc}$ , (b)  $J_{sc}$ , (c) FF, and (d) PCE.

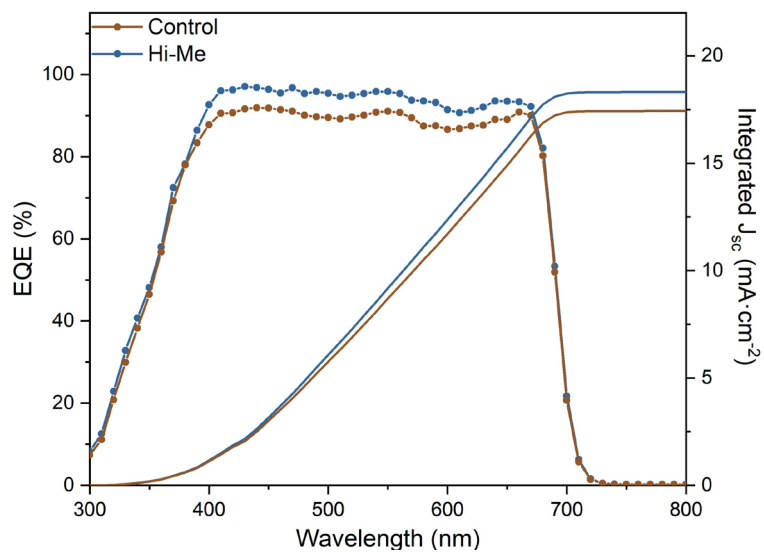


**Figure S3.** EQE curves and integrated  $J_{sc}$  of 1.77 eV-based WBG PSCs based on Me-4PACz and Hi-Me.

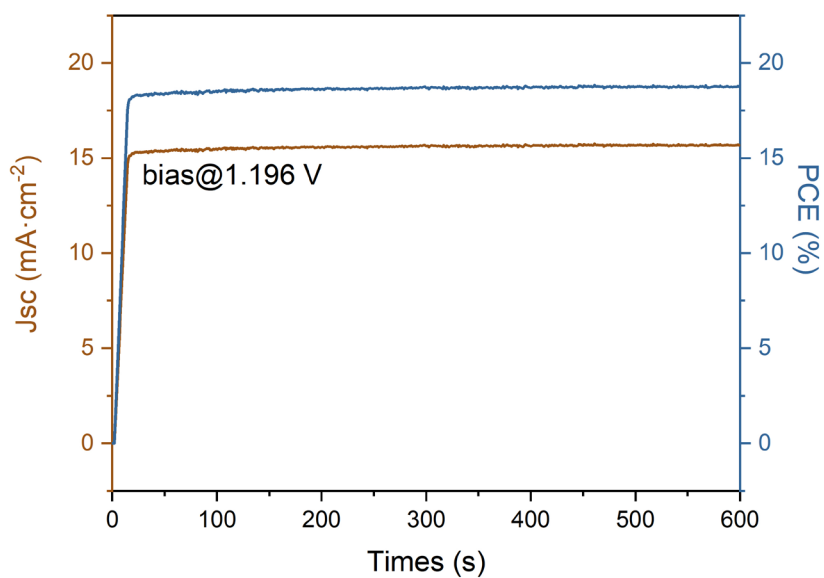


**Figure S4.** Steady-state output performance of champion 1.83 eV-based WBG PSCs.

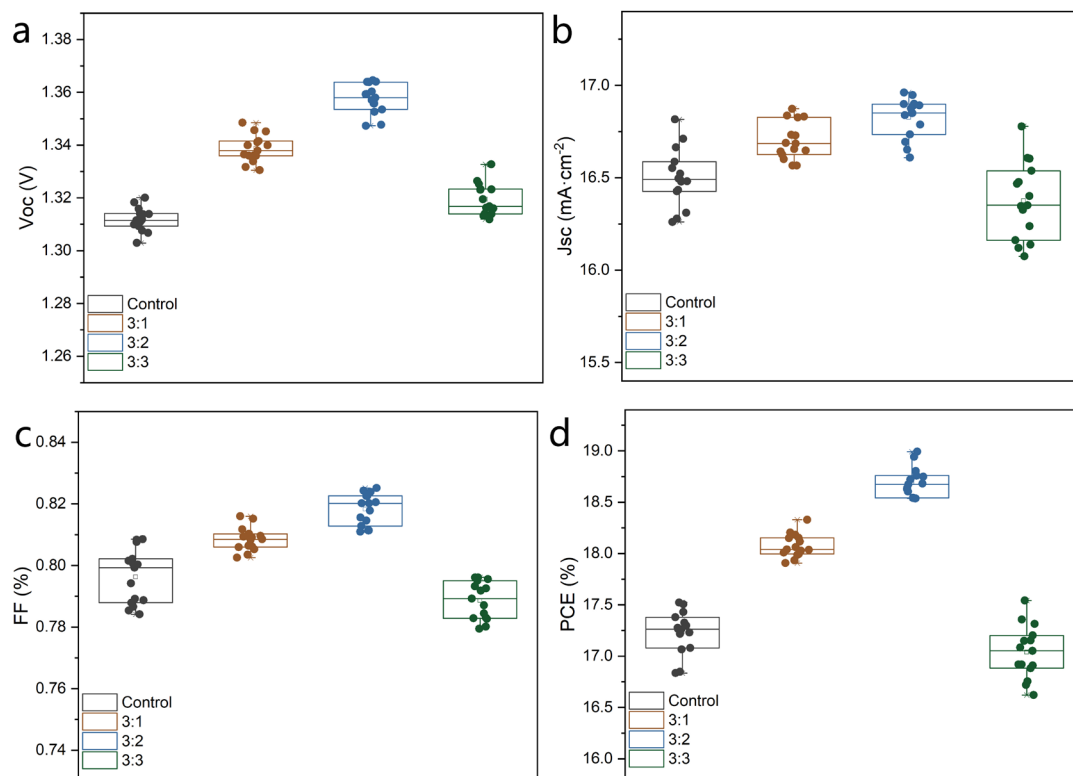


**Figure S5.** Statistical distributions of 1.83 eV-based devices with different ratio of Me-4PACz to Histamine: (a)  $V_{oc}$ , (b)  $J_{sc}$ , (c) FF, and (d) PCE.

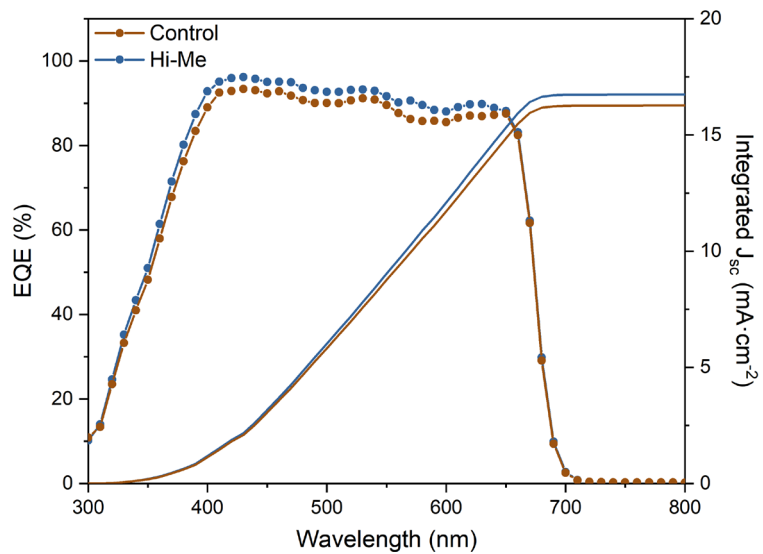


**Figure S6.** EQE curves and integrated  $J_{sc}$  of 1.83 eV-based WBG PSCs based on Me-4PACz and Hi-Me.

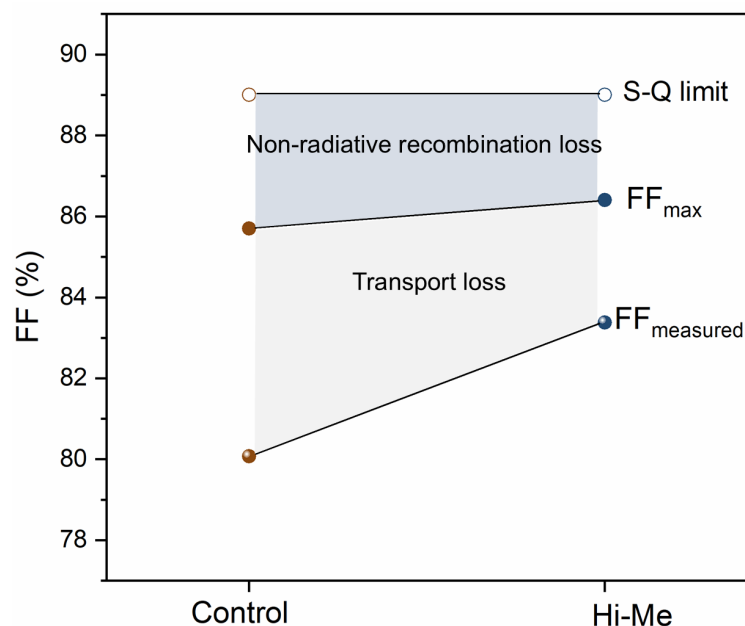


**Figure S7.** The FF S-Q limit of devices, consisting of charge-transport loss and non-radiative recombination loss.

As reported, the primary reasons for the FF values falling below the Shockley-Queisser (S-Q) limit are the trap-assisted non-radiative recombination losses and charge transport losses. the maximum FF ( $FF_{\max}$ ) without charge transport loss can be empirically calculated with the followed equation:

$$FF_{\max} = \frac{\frac{V_{oc}}{nk_B T/q} - \ln\left(\frac{V_{oc}}{nk_B T/q} + 0.72\right)}{\frac{V_{oc}}{nk_B T/q} + 1}$$

Based on  $n_{ID}$  calculations, the maximum FF ( $FF_{\max}$ ) of devices based on Me-4PACz and Hi-Me is determined to be 85.7% and 86.4%, respectively.<sup>1</sup> The modification of buried interface reduce both non-radiative recombination losses and charge transport losses within the devices.

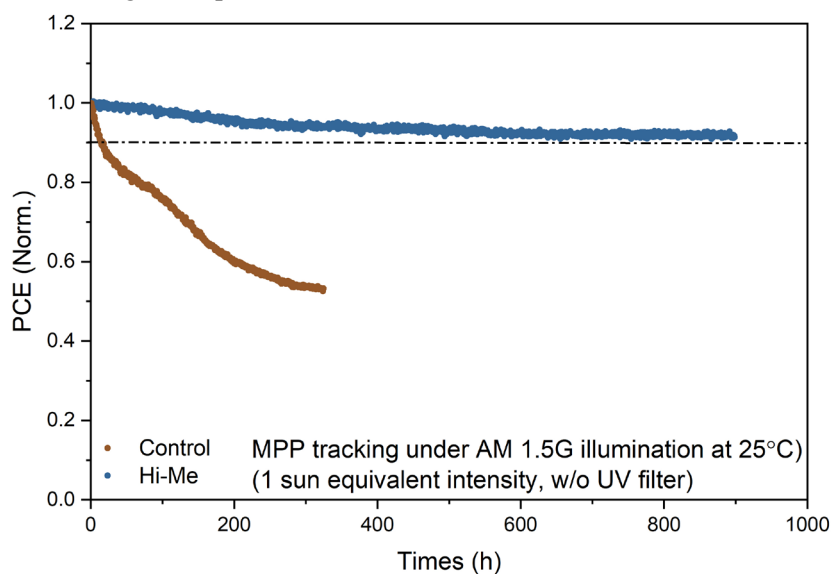


**Figure S8.** Long-term MPP tracking of encapsulated 1.83 eV -based devices under simulated AM 1.5G illumination ( $100 \text{ mW} \cdot \text{cm}^{-2}$  without UV filter),  $25^\circ\text{C}$  in an  $\text{N}_2$ -filled chamber.

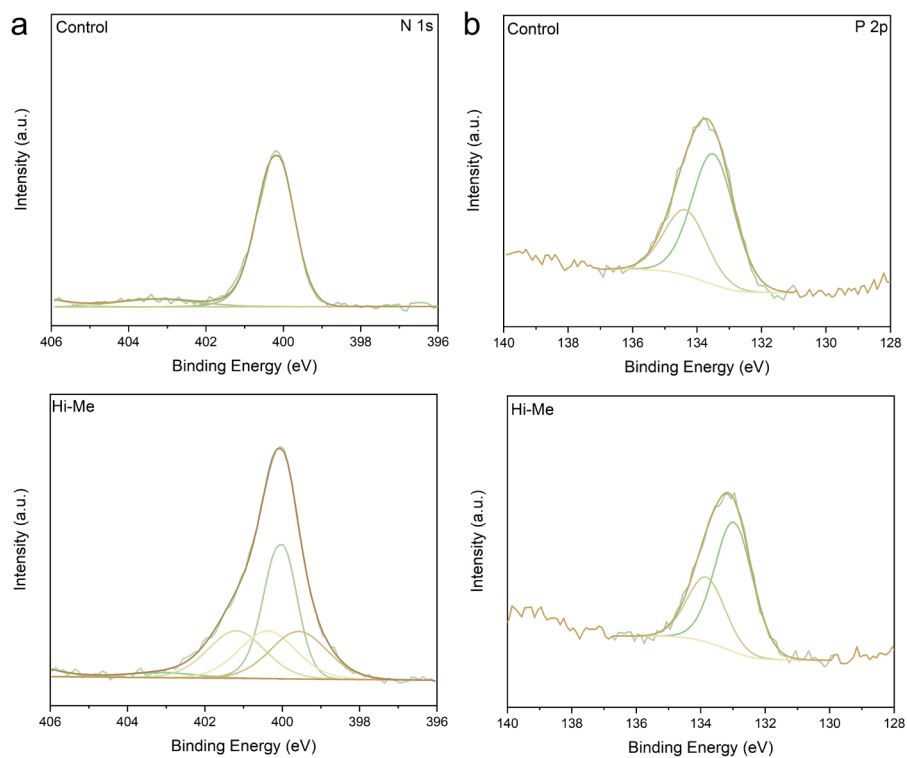


**Figure S9.** (a) N 1s and (b) P 2p XPS spectra of Me-4PACz (upper) and Hi-Me (lower).

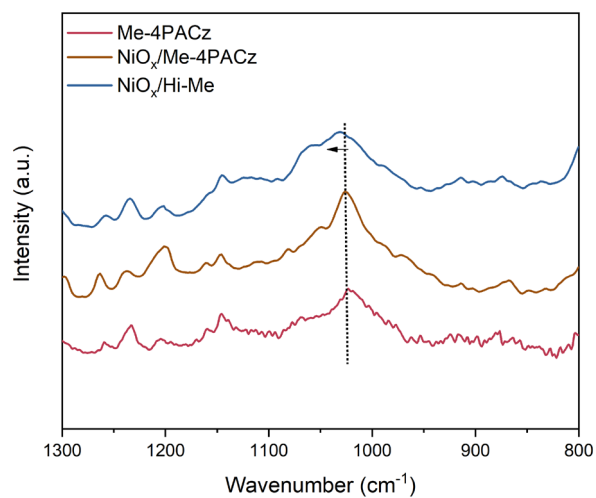


**Figure S10.** ATR-FTIR of pure Me-4PACz, Me-4PACz and Hi-Me SAMs on NiO<sub>x</sub>.

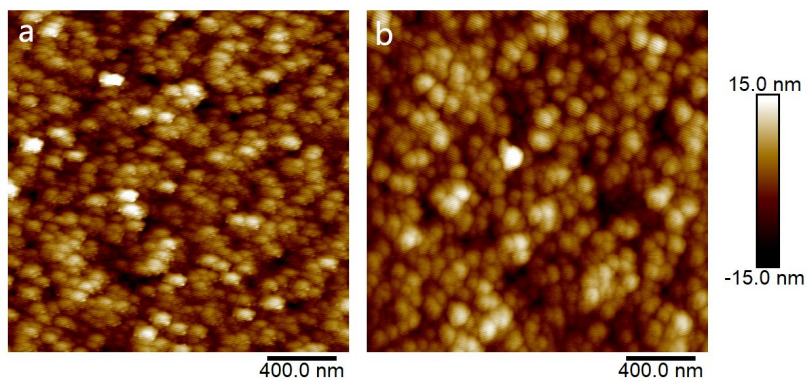


**Figure S11.** AFM images of (a) Me-4PACz and (b) Hi-Me SAMs on ITO/NiO<sub>x</sub>.

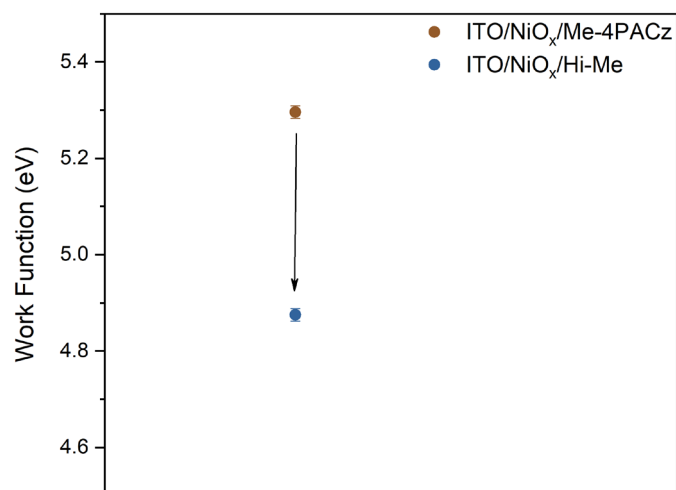


**Figure S12.** Kelvin probe measurements of Me-4PACz and Hi-Me SAMs on ITO/NiO<sub>x</sub>.

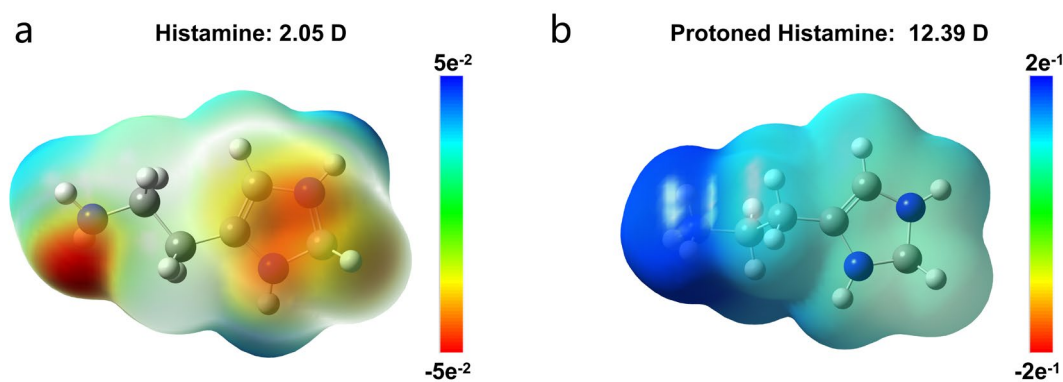


**Figure S13.** Dipole moment of Histamine and protonated Histamine.

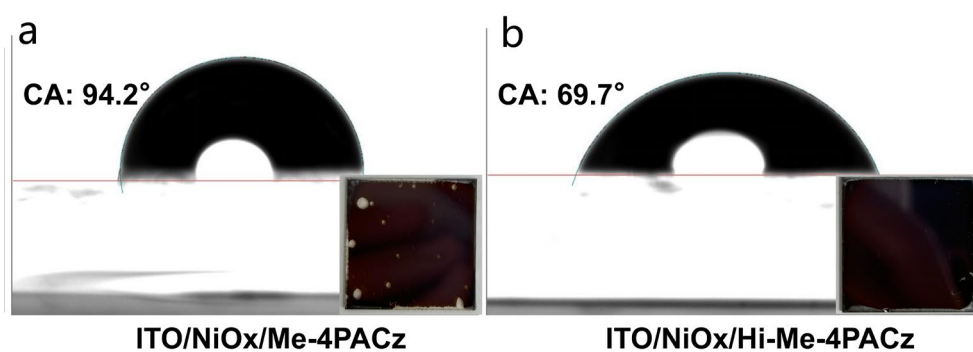


**Figure S14.** Water contact angle of Me-4PACz and Hi-Me film on NiO<sub>x</sub>.

In comparison to 2PACz and MeO-2PACz, the surface wettability of Me-4PACz is much inferior, which adversely affects perovskite crystallization and leads to unsatisfactory film quality with nanovoids. Contact angle measurements show that the surface wettability of Hi-Me is superior to that of Me-4PACz, thereby improving the coverage and uniformity of the perovskite film.

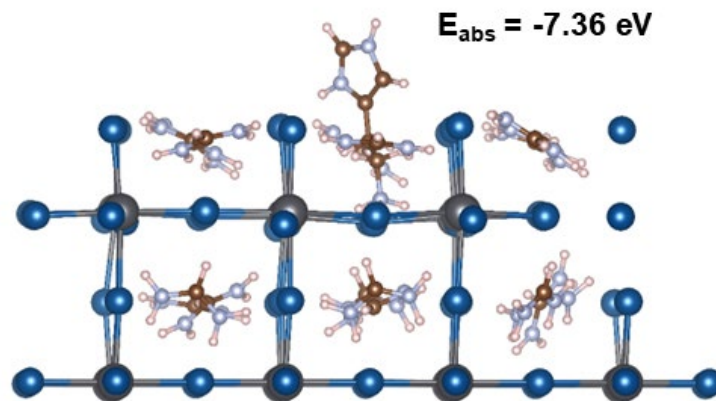


**Figure S15.** Geometry-optimized structures of protonated Histamine on formamidinium vacancies ( $V_{\text{FA}}$ ).

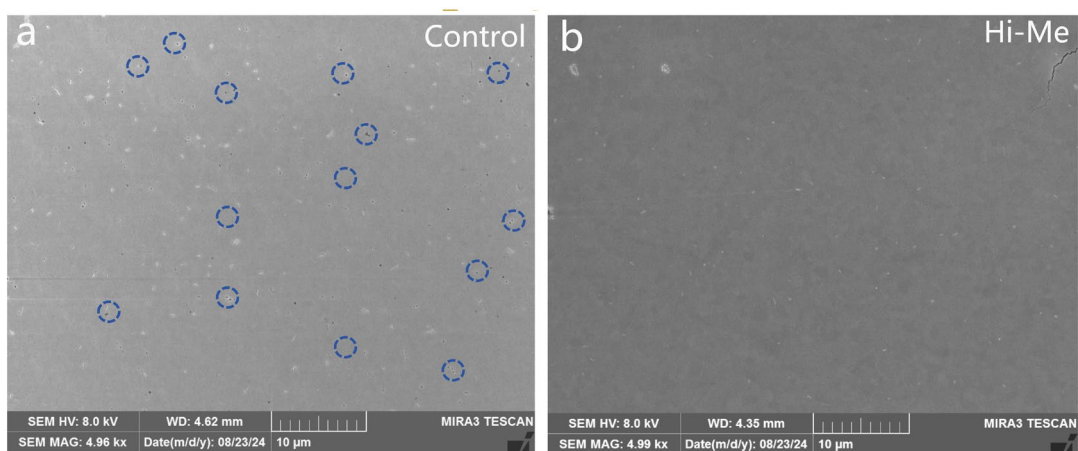


**Figure S16.** Bottom surface SEM images of perovskite films deposited on (a) Me-4PACz and (b) Hi-Me.

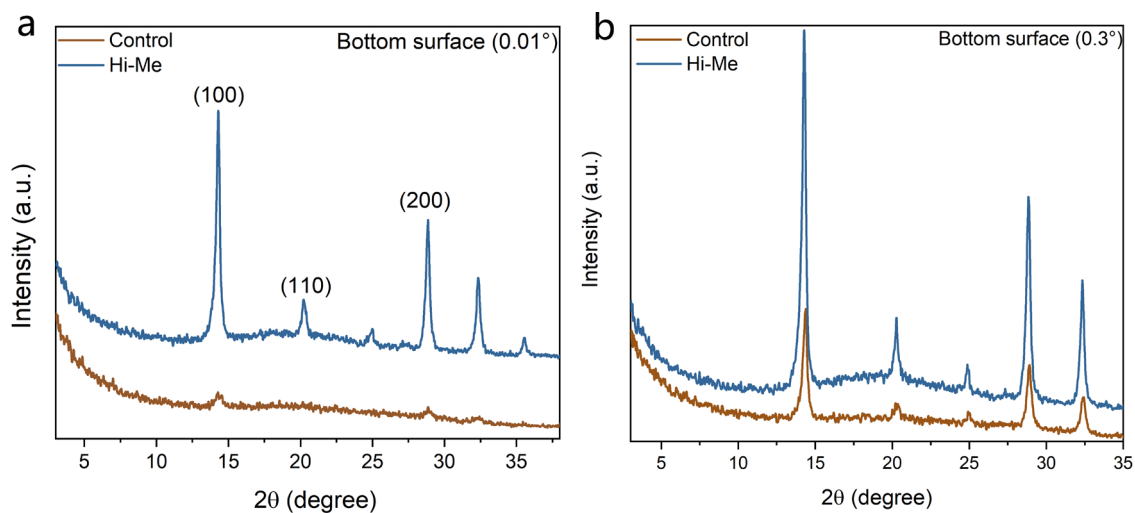


**Figure S17.** Grazing-incidence X-ray diffraction (GIXRD) patterns of bottom surface with the incident angle of (a)  $0.01^\circ$  and (b)  $0.3^\circ$ .

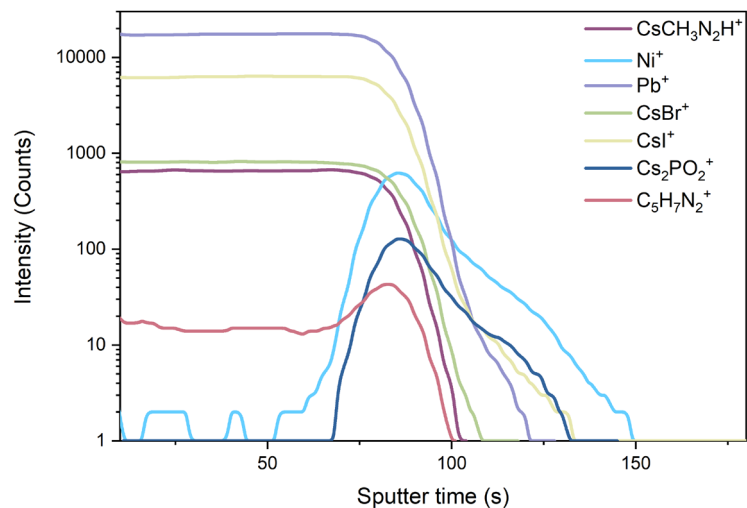


**Figure R18.** Time-of-Flight Secondary Ion Mass Spectrometry of perovskite film fabricated on ITO/NiO<sub>x</sub>/Hi-Me.

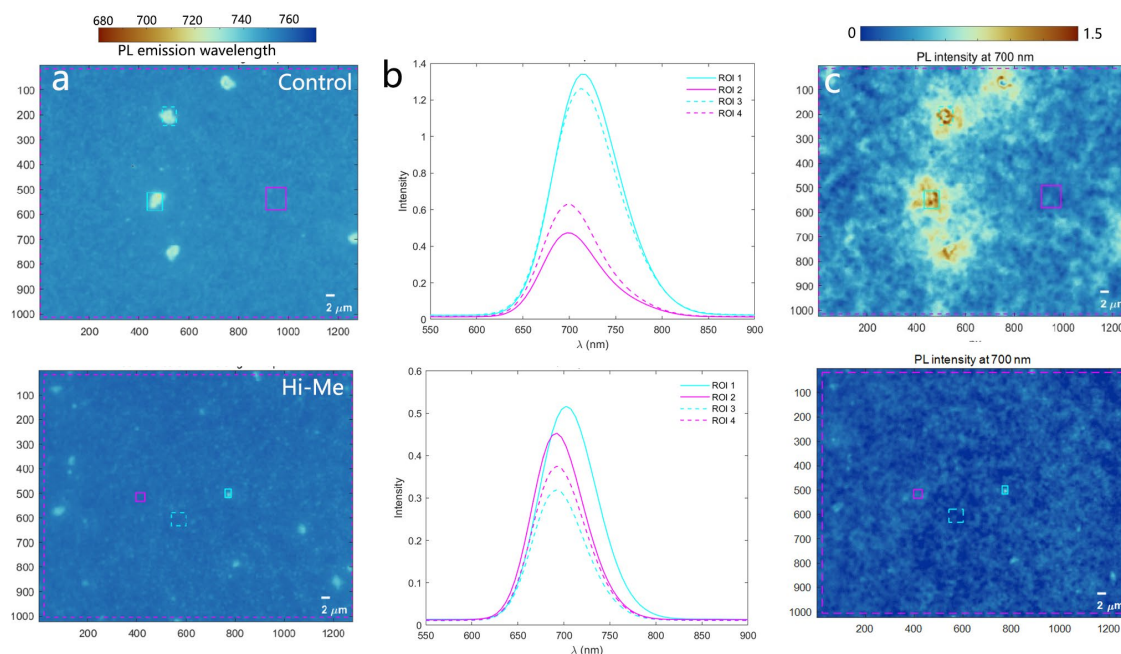


**Figure S19.** (a) Hyperspectral mapping, (b) PL spectra of the marked region, (c) PL intensity mapping at 700 nm of perovskite films deposited on Me-4PACz (upper) and Hi-Me (lower).

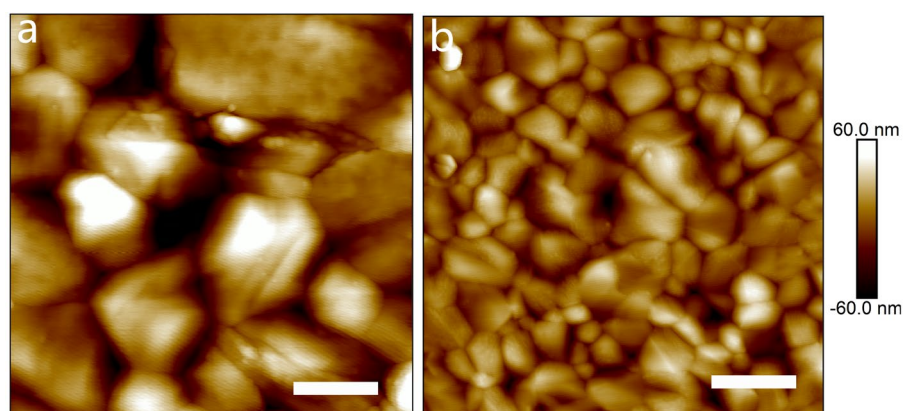


**Figure S20.** AFM images of perovskite films deposited on (a) Me-4PACz and (b) Hi-Me (the scale bar is 1 μm).

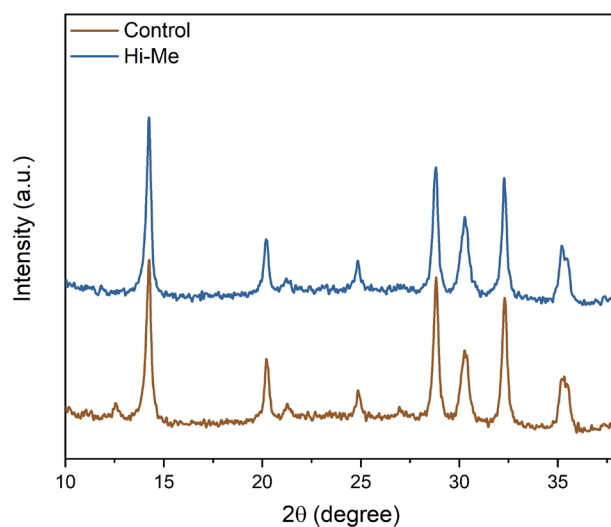


**Figure S21.** Grazing-incidence X-ray diffraction (GIXRD) patterns of top surface.

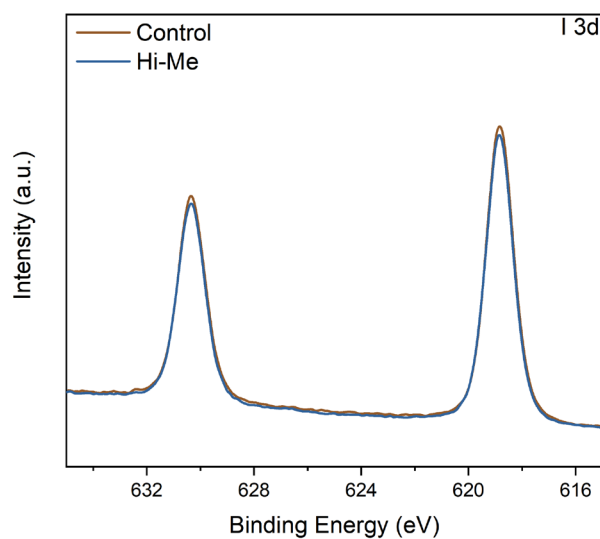


**Figure S22.** I 3d XPS spectra of bottom surface of perovskite film deposited on Me-4PACz and Hi-Me.

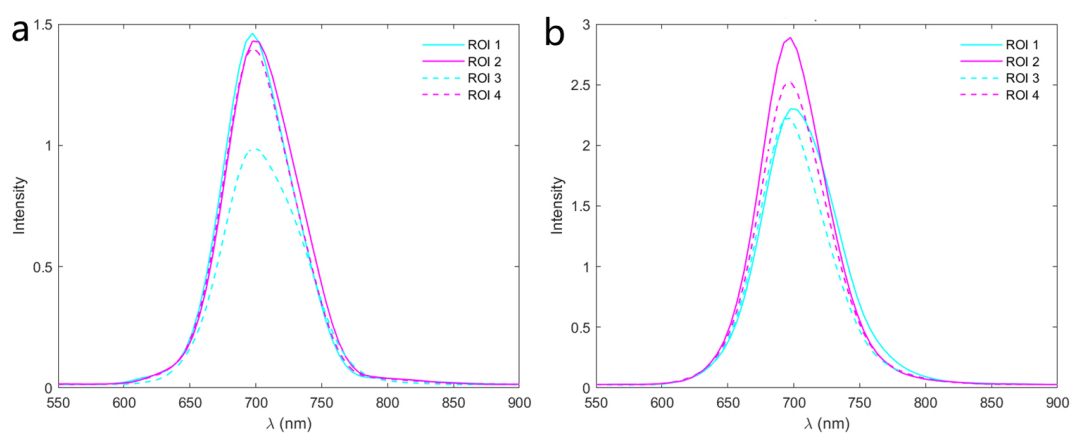


**Figure S23.** PL spectra of the marked region from the Hyperspectral mapping (Figure 4b-c) of the bottom surface of perovskite film deposited on (a) Me-4PACz and (b) Hi-Me.

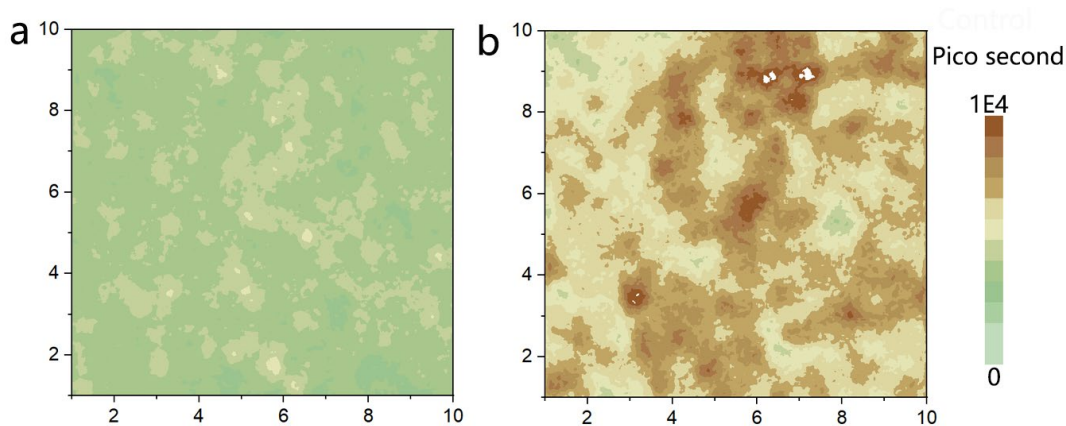


**Figure S24.** Laser confocal fluorescence lifetime mapping obtained by exciting the full devices from the bottom surface based on (a) Me-4PACz and (b) Hi-Me.

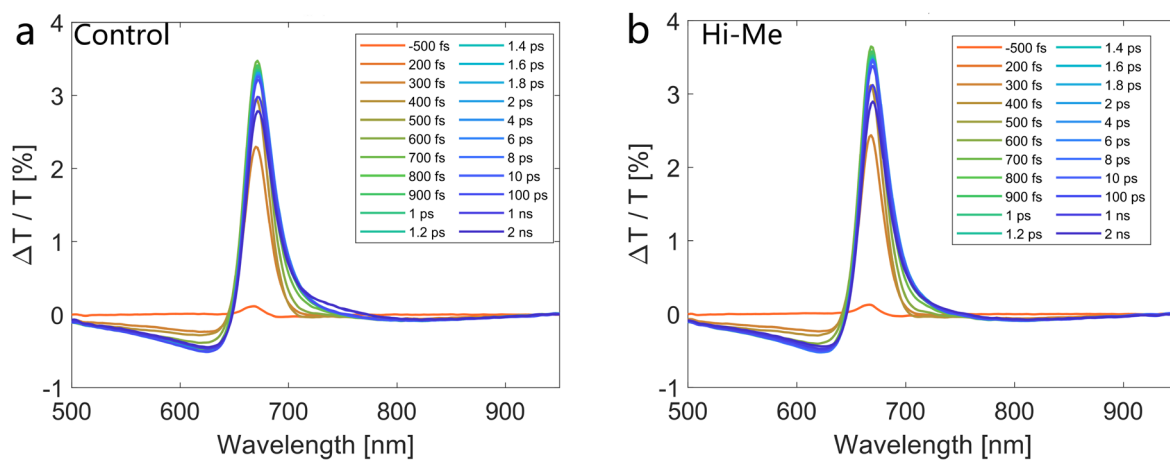


**Figure S25.** Transient absorption spectra of perovskite films deposited on (a) Me-4PACz and (b) Hi-Me (excitation density  $\approx 5.8 \times 10^{17} \text{ cm}^{-3}$ ).

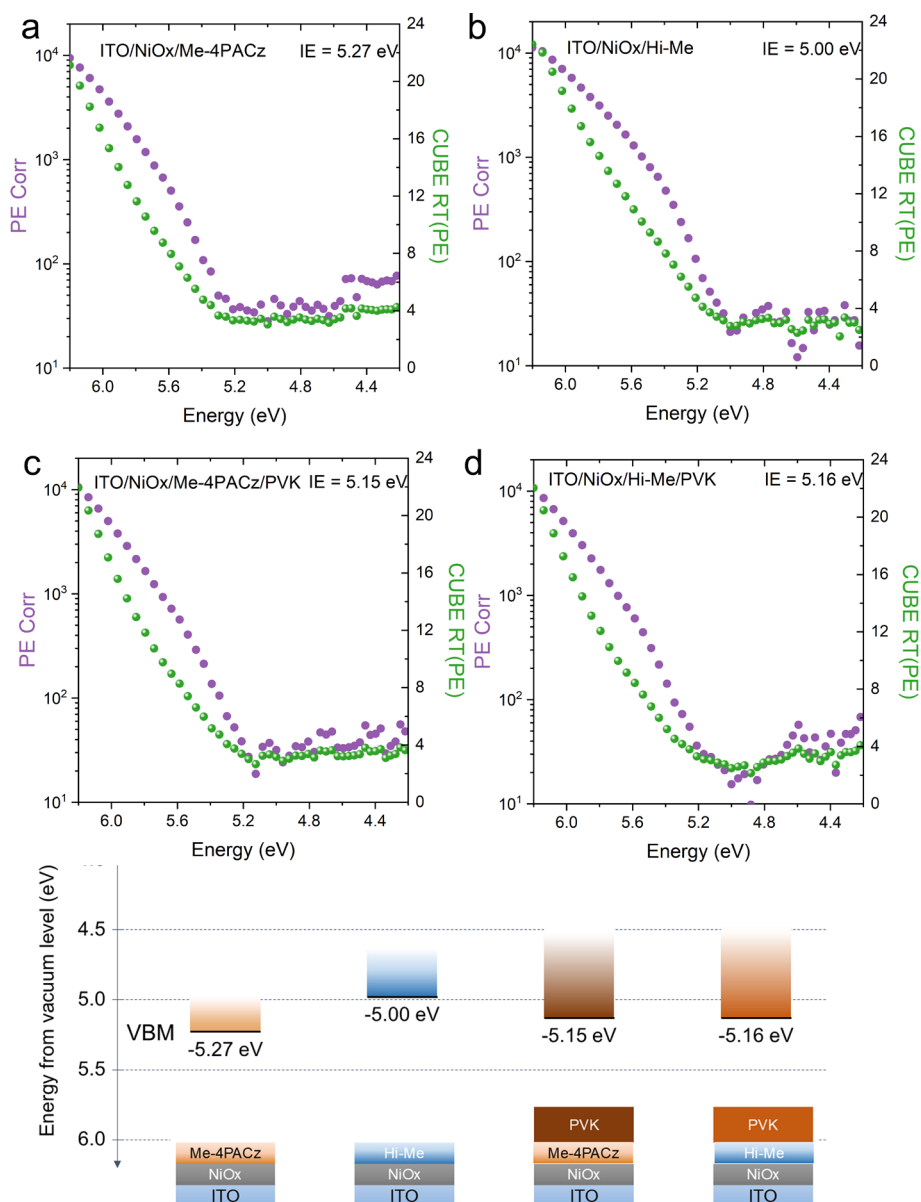


**Figure S26.** Ambient photoemission spectra (APS) and energy-level alignment of Me-4PACz and Hi-Me, as well as perovskite films deposited on Me-4PACz and Hi-Me substrates.

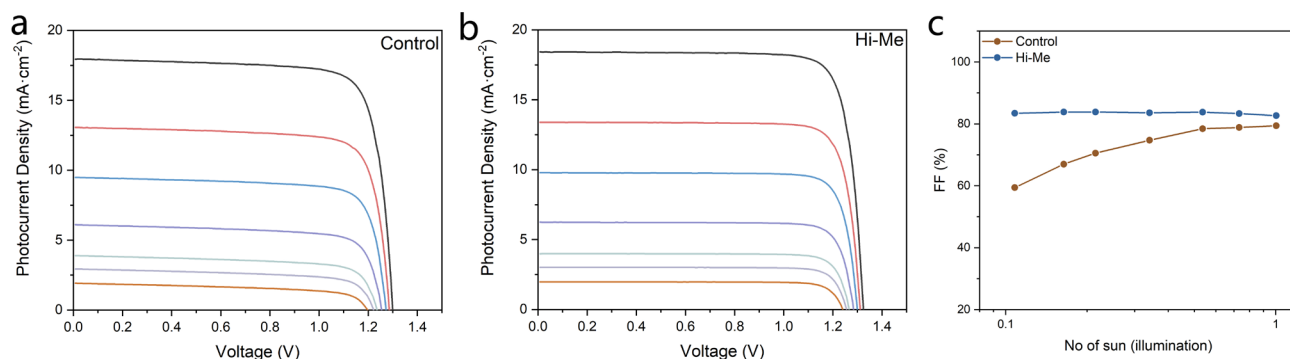


**Figure S27.**  $J$ - $V$  curves of devices based on (a) Me-4PACz and (b) Hi-Me under different light intensity. (c) The FF extracted from the  $J$ - $V$  curves under different light intensity.

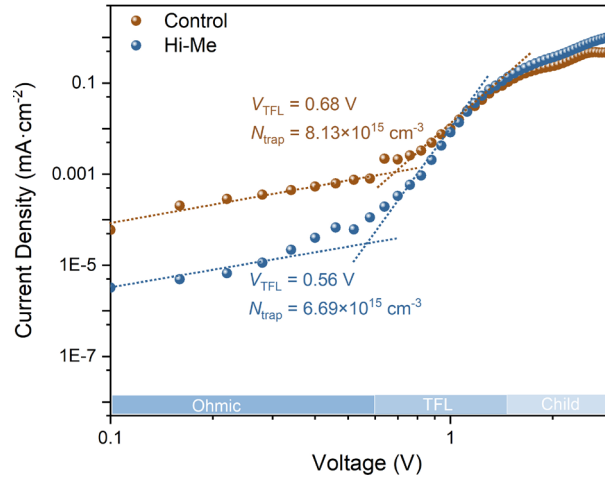


**Figure S28.** SCLC curves of hole-only devices based on based on Me-4PACz and Hi-Me.

Then we performed space-charge limited current (SCLC) measurements using hole-only devices with the structure of ITO/NiO<sub>x</sub>/SAMs/perovskite/PTAA/Au (Figure S28) to estimate the defect density of the perovskite films. The trap-filled limit voltage ( $V_{TFL}$ ) was used to quantitatively estimate the trap state density ( $N_t$ ) based on the following equation:

$$N_t = \frac{2\varepsilon_0\varepsilon_r V_{TFL}}{qL^2}$$

$\varepsilon_0$  and  $\varepsilon_r$  represent the vacuum permittivity and relative dielectric constant, respectively, while  $q$  is the elemental charge and  $L$  is the thickness of perovskite films.<sup>2</sup> The calculated trap density was reduced from  $8.13 \times 10^{15}$  to  $6.69 \times 10^{15} \text{ cm}^{-3}$ , indicating less defects distributed within the devices based on Hi-Me.

**Reference:**

1. J. Wang, J. Zhang, Y. Zhou, H. Liu, Q. Xue, X. Li, C.-C. Chueh, H.-L. Yip, Z. Zhu and A. K. Y. Jen, *Nature Communications*, 2020, 11, 177.
2. Wu, Y. Yan, J. Yin, K. Jiang, F. Li, Z. Zeng, S.-W. Tsang and A. K. Y. Jen, *Nature Energy*, 2024, 9, 411-421.